Report

Current Biology

Rho of Plants GTPases and Cytoskeletal Elements Control Nuclear Positioning and Asymmetric Cell Division during *Physcomitrella patens* Branching

Graphical Abstract

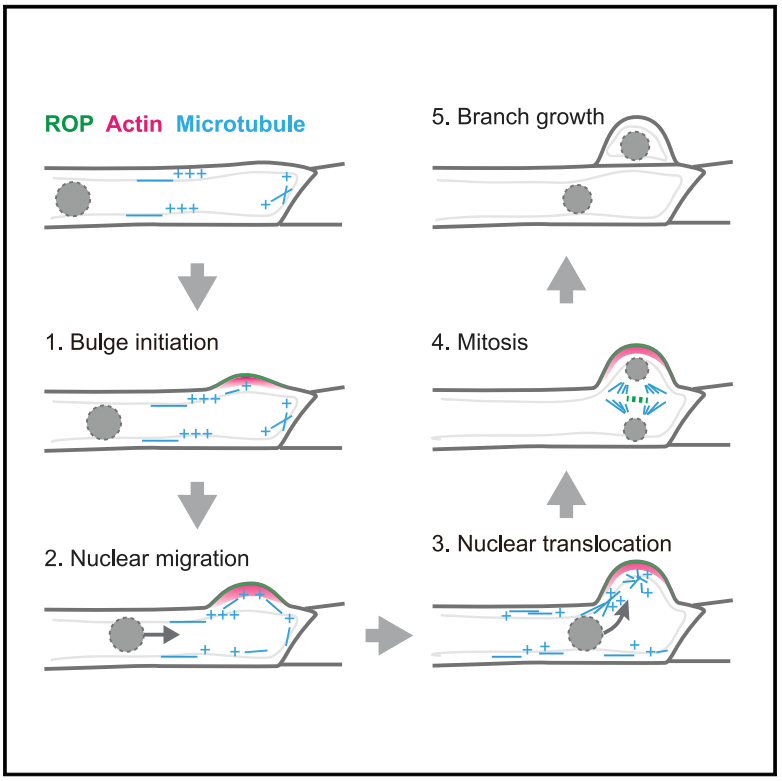

Authors

Peishan Yi, Gohta Goshima

Correspondence

yi.peishan@a.mbox.nagoya-u.ac.jp

In Brief

Yi and Goshima investigate branch initiation in the moss *P. patens* protonemata. The study shows that ROP GTPases and actin initiate the formation of polarized bulges in the pre-branching cells, which in turn directs microtubule-dependent nuclear migration and subsequent asymmetric cell division.

Highlights

- MTs are essential for nuclear migration but are less involved in bulge formation
- Bulge formation alters microtubule patterning and guides nuclear migration
- ROP GTPases and actin play an essential role in bulge initiation
- ROP4 is localized to the apical membrane and the assembling cell plate

Yi & Goshima, 2020, Current Biology *30*, 2860–2868
July 20, 2020
https://doi.org/10.1016/j.cub.2020.05.022

CellPress

CellPress

Current Biology

Report

Rho of Plants GTPases and Cytoskeletal Elements Control Nuclear Positioning and Asymmetric Cell Division during *Physcomitrella patens* Branching

Peishan Yi[1,3,*] and Gohta Goshima[1,2]

[1]Division of Biological Science, Graduate School of Science, Nagoya University, Furo-cho, Chikusa-ku, Nagoya 464-8602, Japan

[2]Sugashima Marine Biological Laboratory, Graduate School of Science, Nagoya University, Sugashima-cho, Toba 517-0004, Japan

[3]Lead Contact

*Correspondence: yi.peishan@a.mbox.nagoya-u.ac.jp

https://doi.org/10.1016/j.cub.2020.05.022

SUMMARY

Branching morphogenesis is a widely used mechanism for development [1, 2]. In plants, it is initiated by the emergence of a new growth axis, which is of particular importance for plants to explore space and access resources [1]. Branches can emerge either from a single cell or from a group of cells [3–5]. In both cases, the mother cells that initiate branching must undergo dynamic morphological changes and/or adopt oriented asymmetric cell divisions (ACDs) to establish the new growth direction. However, the underlying mechanisms are not fully understood. Here, using the bryophyte moss *Physcomitrella patens* as a model, we show that side-branch formation in *P. patens* protonemata requires coordinated polarized cell expansion, directional nuclear migration, and orientated ACD. By combining pharmacological experiments, long-term time-lapse imaging, and genetic analyses, we demonstrate that Rho of plants (ROP) GTPases and actin are essential for cell polarization and local cell expansion (bulging). The growing bulge acts as a prerequisite signal to guide long-distance microtubule (MT)-dependent nuclear migration, which determines the asymmetric positioning of the division plane. MTs play an essential role in nuclear migration but are less involved in bulge formation. Hence, cell polarity and cytoskeletal elements act cooperatively to modulate cell morphology and nuclear positioning during branch initiation. We propose that polarity-triggered nuclear positioning and ACD comprise a fundamental mechanism for increasing multicellularity and tissue complexity during plant morphogenesis.

RESULTS AND DISCUSSION

The branched filamentous growth of moss *P. patens* is an excellent system to study branching morphogenesis [6]. We visualized the protonema subapical cell branching using long-term time-lapse imaging [7] (Video S1). Following apical cell division, the nucleus of the first subapical cell moved toward the cell center and was transiently positioned at a point 36% (51.8 ± 8.5 μm [±SD, n = 69]) of the cell length from the apical end. Around 9.2 ± 1.7 h (±SD, n = 50) after apical cell division, a membrane subdomain at the distal end started to bulge. Meanwhile, the nucleus was slowly moving toward the apical end or remained static, but never moved backward. During bulging, the nucleus moved progressively toward the bulge. When it approached the bulge, bundles of microtubules (MTs) appeared to connect the base of the bulge and the migrating nucleus (Figure 1A), which was followed by rapid translocation of the nucleus into the bulge, nuclear envelope breakdown (NEB), and mitosis. The division plane was aligned along the apical-basal axis, thus producing a side-branch initial cell. The average velocity of nuclear migration and bulge growth before division was 3.3 ± 1.8 μm/h (±SD, n = 28) and 3.3 ± 1.5 μm/h (±SD, n = 17), respectively. However, their values in single cells were not positively correlated, suggesting that nuclear migration and bulge growth were not tightly coupled. Given that steady nuclear migration occurred slightly later than bulge initiation (0.9 ± 0.9 h [±SD, n = 36]) and was always observed during bulging, we concluded that a signal from the bulge was required to guide nuclear movement, but transduction of this signal is not instant.

Coincident cell growth and nuclear positioning have been observed in multiple plant systems; however, their relationship is controversial. In ferns, nuclear position modification by centrifugation alters branch site selection, suggesting that the nucleus, together with associated cytoplasmic materials, may produce a cue for branch initiation [8]. In flowering plants, polar growth of root hairs can be dependent or independent of nuclear positioning [9–11]. In *P. patens*, blocking MT dynamics inhibits nuclear migration, but not branch initiation, suggesting that branch initiation is upstream of nuclear positioning [12]. However, MTs are also required for cell growth in both tip and subapical cells [12–14]. To further investigate the roles of MTs in bulge formation and nuclear migration, we used oryzalin to disrupt the MT network. When supplemented with ≥5 μM oryzalin, almost all subapical cells did not enter mitosis. At 5 μM, MTs were undetectable in 83% (n = 29) of the caulonemal cells (Figure S1A). On the other hand, oryzalin at 1 μM did not block the mitotic entry of

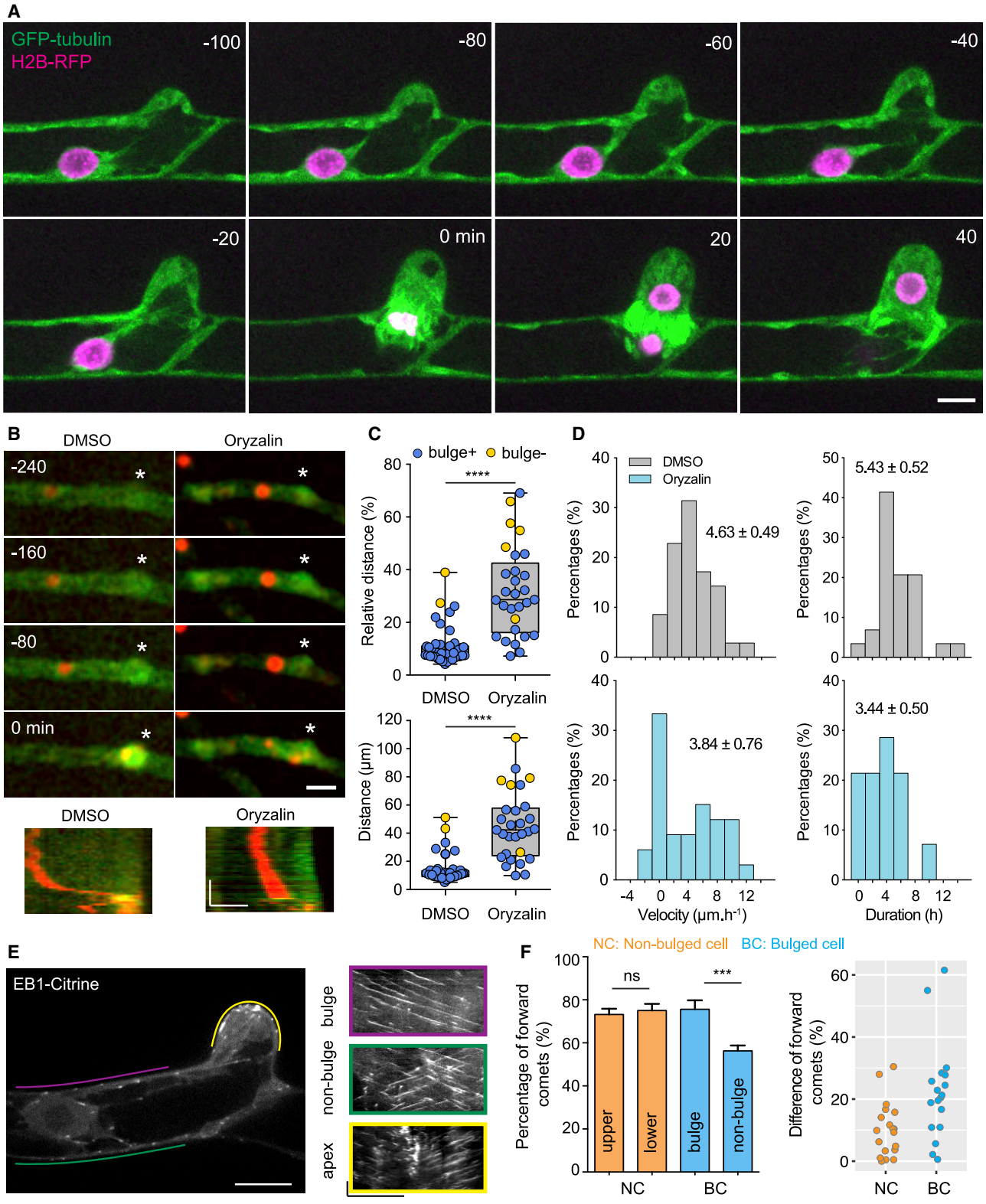

Figure 1. MTs Drive the Long-Distance Nuclear Migration during Subapical Cell Branching

(A) Bulging, nuclear migration, and asymmetric division in a wild-type subapical cell labeled with GFP-tubulin (green) and H2B-RFP (magenta). 0 min, nuclear envelope breakdown (NEB). Scale bar, 10 µm.

(legend continued on next page)

the subapical cells, despite the fact that MTs were not detected in 62% (n = 40) of the cells and the remaining cells had substantially fewer and shorter MTs (Figure S1A). However, spindle assembly was completely blocked, leading to chromosome scattering after NEB (Figure 1B; Video S2). In control cells, nuclei were positioned at a distance of 13.7 ± 1.4 μm (11% of cell length [±SEM, n = 44]) from the apical end, whereas a significant defect was observed in oryzalin-treated cells with their nuclei positioned at a distance of 45.4 ± 4.5 μm (32% of cell length [±SEM, n = 29]) (Figure 1C). This defect was caused by a combined effect of reduced migration velocity and duration (Figure 1D). Interestingly, 83% of the cells treated with oryzalin initiated a bulge at the distal end regardless of their nuclear positions (Figure 1C). These results indicate that MTs are essential for long-distance nuclear transport, but are less involved in bulge formation. More importantly, nuclear position is not a prerequisite of branch site selection in *P. patens*.

We next asked whether bulge formation indeed guides nuclear migration. We used latrunculin A (LatA) to disrupt the actin network as actin accumulates at the bulging site [15–18]. Similar to oryzalin treatment, high concentration (≥10 μM) of LatA inhibited cell-cycle progression. At 5 μM, although actin filaments were undetectable in the majority of the caulonemal cells (77%, n = 31; Figure S1B) and tip cell growth was completely blocked, the mitotic entry of subapical cells appeared normal. We thus created a situation where bulged and non-bulged cells were present roughly at an equal frequency (56% versus 44%), which allowed us to examine the roles of actin and bulge in nuclear migration and subapical cell division (Figure 2A; Video S3). In LatA-treated cells, nuclei prior to NEB were positioned at a distance of 40.7 ± 4.5 μm (22% of cell length [±SEM, n = 36]) from the apical end, which was much further than nuclei of control cells (15.3 ± 2.8 μm, 9% of cell length [±SEM, n = 23]) (Figure 2B). Division planes in migration-deficient cells became perpendicular to the longitudinal axis (Figure 2A). Interestingly, almost all bulge-forming cells could position their nuclei toward the distal end; however, division planes in many cells were unable to orient along the apical-basal axis (Figure 2C), which was likely due to the inhibition of bulge growth, but not initiation. In non-bulged cells, nuclei exhibited random movement before mitosis. The rapid migrating phase before NEB, which was absent in oryzalin-treated cells, was still observable (Figure 2A). The nuclear migration speed of LatA-treated cells was significantly lower than that of control cells (0.3 ± 0.3 μm/h [±SEM, n = 49] in LatA cells, 4.0 ± 0.4 μm/h [±SEM, n = 18] in control cells) (Figure 2D). Using high-resolution microscopy, we confirmed that LatA treatment after bulge initiation inhibited bulge growth but had little effect on nuclear positioning (Figure 2E), suggesting that bulge initiation and nuclear migration are tightly coupled. However, the nucleus could not enter the immature bulge due to space limitation. Consequently, the division plane was positioned in the apical cytoplasm and became more perpendicular. These results, together with the observation that nuclear migration deficiency does not evidently affect bulge formation (Figures 1B and 1C), suggest that actin-dependent bulge formation acts upstream to regulate MT-dependent nuclear movement.

The relationship between bulge formation and nuclear positioning raises the possibility that cell geometry regulates MT patterning. To test this hypothesis, we examined the dynamics of MTs using the plus-end binding protein EB1 [19, 20]. Since the cytoplasm of subapical cells is occupied by a large vacuole, we imaged EB1 comets in the lateral cytoplasm between the vacuole membrane and cell wall along the apical-basal axis (Figure 1E). Before bulging, growing MTs were predominantly oriented toward the apical end with 73% and 75% (n = 19 cells) forward comets at the upper and lower side of the cell (regions labeled by magenta and green lines in Figure 1E), respectively (Figure 1F). When the bulge had partially formed and the nucleus had not reached the bulge, MTs on the bulge side maintained biased orientation with 76% (in 18 cells) comets toward the apical end, while only 56% of MTs on the non-bulge side grew forward (Figure 1F). Meanwhile, convergent MTs were detected at the apex of the growing bulge (Figure 1E). Biased orientation and convergence of MTs were also observed at the apex of tip cells, indicating that orientated MT network at the apex is a general feature in *P. patens* [19]. However, LatA treatment after bulge initiation did not affect MT patterning (Figure 2F), suggesting that immature bulge is sufficient to induce nuclear migration. In tip cells, LatA also had no effects on MT orientation but inhibited MT-actin foci formation [14, 21]. Given that MT is not essential for bulge formation, our results suggest that patterning of MTs is responsive to geometrical changes and may account for nuclear migration. Particularly, as nuclear positioning in *P. patens* requires antagonistic action of opposite-directed kinesin motors [20–22], change of MT patterning could break such a balance, thus leading to directed nuclear movement. However, the role of MTs in bulge formation cannot be entirely excluded, as biased MT growth might be initiated to some degree at one side of the cytoplasm before bulge formation and contribute to bulge growth (Figure 1F, right).

Bulge initiation requires a polarized organization of actin [16]. We speculate that polarity proteins, such as the Rho of plants (ROP) GTPase, could be a critical regulator [23]. *P. patens* genome encodes four *rop* genes [24, 25]. The knockdown of all four *rop* genes by RNAi leads to severe growth defects and round cells, making it difficult to examine their roles in branching

(B) 1 μM oryzalin inhibits nuclear migration, but not bulge formation, in long-term imaging. Control cells were treated with DMSO. Stars indicate bulge formation. Scale bars, 20 μm (horizontal), 2 h (vertical).

(C) Box-and-whisker plots of division site positioning along the apical-basal axis after NEB. Boxes show the interquartile range. Median and mean values are indicated by the crossline and "+," respectively. Bulged and non-bulged cells are colored in blue and yellow, respectively. DMSO, n = 44; oryzalin, n = 29. ****$p < 0.0001$.

(D) Histogram of nuclear migration velocity (DMSO, n = 35; oryzalin, n = 33) and duration (DMSO, n = 29; oryzalin, n = 28).

(E) EB1 dynamics in branching subapical cells. Kymographs generated from colored lines show the direction of growing MTs in the corresponding cytoplasmic regions. Scale bars, 10 μm (horizontal), 1 min (vertical).

(F) Quantification of forward EB1 comets in non-bulged (NC) and bulged cells (BC). The right panel shows the difference of forward EB1 comets in the two cytoplasmic regions (10% ± 2% versus 22% ± 4%, ± SEM). Non-bulged cell, n = 19 cells; bulged cell, n = 18 cells. Mean ± SEM; ns, not significant. ***$p < 0.001$. See also Figure S1 and Videos S1 and S2.

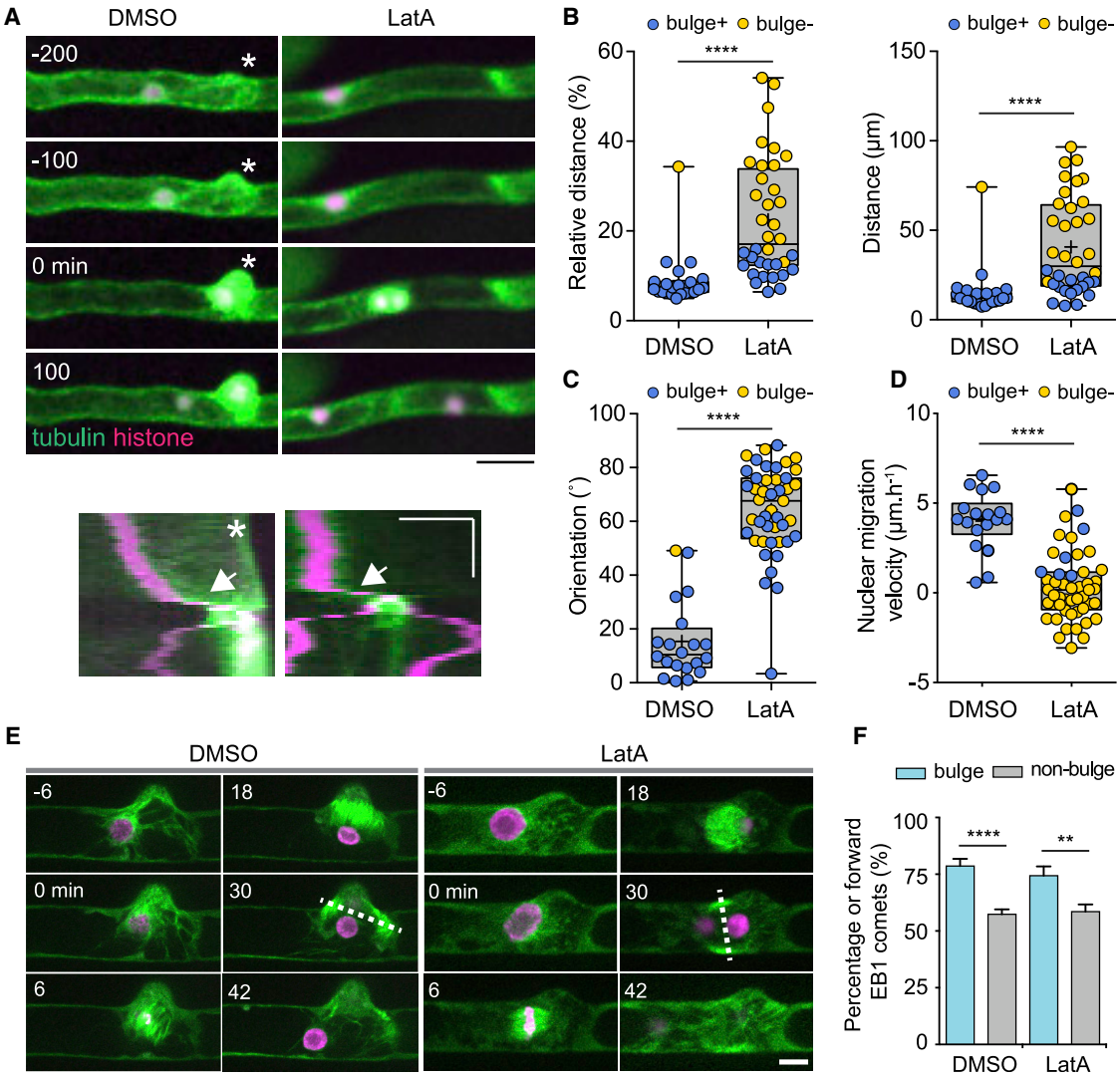

Figure 2. Actin Is Essential for Bulge Formation and Nuclear Migration

(A) 5 μM latrunculin A (LatA) inhibits bulge formation and nuclear migration. Control cells were treated with DMSO. Stars indicate bulge formation. Arrows indicate the fast nuclear movement before NEB. 0 min, NEB. Scale bars, 30 μm (horizontal), 3 h (vertical).

(B–D) Box-and-whisker plots of division site positioning along the apical-basal axis (B), the orientation of division plane (C), and nuclear migration velocity (D). Boxes show the interquartile range. Median and mean values are indicated by the crossline and "+," respectively. Bulged and non-bulged cells are colored in blue and yellow, respectively. DMSO, n = 23 (B and C) and 18 (D). LatA, n = 36 (B and C) and 49 (D).

(E) 25 μM LatA inhibits bulge growth and division plane orientation. Dotted lines indicate a division plane. Scale bar, 10 μm.

(F) LatA treatment after partial bulge formation does not affect the biased orientation of growing MTs labeled by EB1 comets. Mean ± SEM. ****$p < 0.0001$. **$p < 0.01$.

See also Figure S1 and Video S3.

[24]. Therefore, we generated hypomorphic mutants using the CRISPR/Cas9 techniques [26, 27]. We obtained single, double, and triple mutants, but failed to generate a quadruple mutant (Figures S2A and S2B). Single and double mutants exhibited mild growth defects (Figures 3A and 3B). Tip cell growth was significantly reduced and cell length was shortened in triple mutants; however, branched filaments were still able to develop (Figures 3C and S2C–S2E). Gametophores were able to grow, but rhizoid growth was markedly decreased (Figure 3E). Introducing a tryptophan-to-arginine mutation of *rop4* in the *rop1-3* mutants resulted in severely shortened and round cells and small gametophores [27], mimicking the RNAi phenotypes [24] (Figure 3D). These results, together with our inability to obtain quadruple knockouts, indicate that ROP is essential for viability.

Because *rop2, rop3, rop4* triple mutants could develop branched filaments and showed a slightly stronger growth phenotype (Figure 3B), we focused on this strain for further analysis. Using time-lapse imaging, we observed defective bulge formation and abnormal subapical cell division, a phenomenon that was frequent in older plants (Figure 3F; Video S4). On average, the division plane was positioned at a distance of 20.0 ± 2.0 μm (22% of cell length [±SEM, n = 37]) from the apical end,

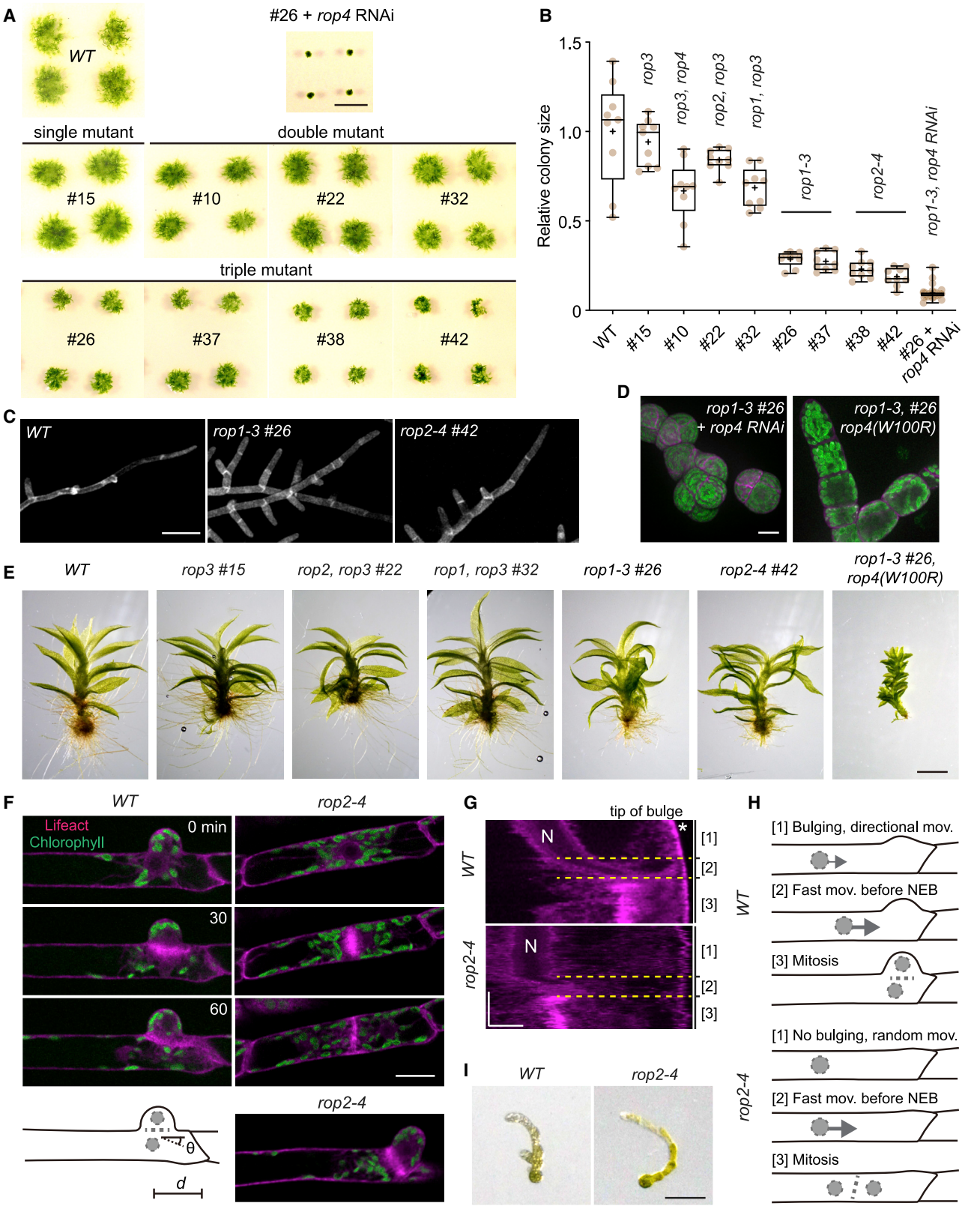

(legend on next page)

which was higher than that in wild-type cells (12.4 ± 1.3 μm, 9% of cell length [±SEM, n = 21]) (Figure S2F). In non-bulged cells, the directional migration of nuclei was impaired, but the fast-moving phase before NEB was retained (Figures 3G, 3H, and S2G). Division planes were mostly aligned in the transverse direction, phenocopying LatA-treated cells (Figures 2A and 3F). In the bulged cells, the orientation of division planes became more oblique (Figure 3F, bottom). Time-lapse analyses revealed little change in the orientation of the phragmoplast throughout cytokinesis, suggesting that the orientation of the division plane in *rop* mutants is defined prior to anaphase by spindle orientation and does not result from a deficiency in phragmoplast guidance (Figures S3I and S3J). To confirm that ROP is required for branching, we examined branch formation in regenerating protoplasts. As shown in Figures 3I and S2H, the formation of the first branch was clearly delayed in the *rop* triple mutants. Because the growth of primary filaments was not affected, these results indicate that branching defect was not a result of overall growth retardation.

Overexpression of ROP causes substantial growth defects [24, 28]. Hence, we expressed ROP1 or ROP4 ectopically under the control of a β-estradiol-inducible promoter to perform a rescue experiment [29]. Intriguingly, basal level expression of ROP1 or ROP4 without β-estradiol induction rescued protonema growth phenotypes in triple mutants, while the addition of 1 μM β-estradiol led to severely shortened and round cells (Figures S2I and S2J). Immunoprecipitation and western blotting confirmed that the expression of ROPs was leaky without induction (Figures S2K and S2L). As identical phenotypes were observed in different triple mutants, our data demonstrated that PpROPs redundantly regulate cell growth and branching. We next asked whether branching defects were caused by the change of cell fate and/or morphology. By quantifying the size of chloroplasts and using a subapical cell-specific reporter (STEMIN1pro:NGG), we verified that the fates of tip cells and subapical cells were not changed in the triple mutants [30] (Figures S3A–S3D). In addition, a mutant *short1*, which was isolated from our UV mutagenesis, exhibited shortened cells and reduced tip growth, but did not show defects in branch formation (Figures S3E–S3G). These data indicate that branching phenotypes in *rop* mutants were not caused by altered cell shape and reduced tip cell growth.

We next examined the subcellular localization of *rop4*, one of the highly expressed *rop* genes [24]. Endogenous tagging of ROP4 with mNeonGreen (mNG), a bright monomeric green fluorescent protein [31], showed cytoplasmic and membrane localization. C-terminal, but not N-terminal, tagging also exhibited nucleolus localization, which was likely an artifact caused by interfering with the C-terminal prenylation signal [25]. For this reason, we used the N-terminal tagging line for subsequent analysis. ROP4 expression was detectable in protonema cells, gametophore initials, and rhizoids, and it showed polar localization at the apical membrane along with the cortical accumulation of actin (Figure 4A). In subapical cells, the accumulation of mNG-ROP4 was evident at the initial bulging stage, supporting its roles in triggering bulge initiation.

In mitotic cells, mNG-ROP4 was detectable at the assembling cell plate (Figure 4B; Video S5). Localization of mNG-ROP4 at the plasma membrane and cell plate depends on its C-terminal prenylation as modifying the CXXL motif abolished this localization pattern (Figure 4C). In *Arabidopsis*, two putative ROP GTPase-activating proteins, PHGAPs, which are related to ROP1 enhancer (REN1), localize at the cortical division zone (CDZ) and participate in division plane orientation [32]. The sole homolog of PHGAPs and REN1 in *P. patens* PpREN does not bind to ROPs, and its loss of function has little effect on protonema growth [33]. PpREN showed localization in the cytoplasm, at the plasma membrane, and at the CDZ during late metaphase and anaphase. However, unlike PHGAPs, it disappeared from the CDZ after cytokinesis (Figure S3H). PpREN accumulation at the CDZ occurred slightly earlier than cell plate attachment (Figure S3H; Video S5). Thus, PpROP might play additional roles in cytokinesis, such as amplifying actin polymerization and/or mediating attachment of the nascent cell plate to the lateral cell wall.

In this study, we revealed the critical roles of ROP GTPases and cytoskeletal elements in *P. patens* branch formation (Figure 4D). Unlike that suggested in ferns [8], branch selection in *P. patens* is epistatic to nuclear positioning. Branch initiation relies on ROP-actin-dependent cell polarization but is likely independent of their roles in regulating cell size. In *Arabidopsis*, polarization and polar growth of root hairs are separate processes employing distinct ROP guanine nucleotide exchange factors (RopGEFs) [34]. The *P. patens* genome encodes six RopGEFs, of which RopGEF4 shows confined localization at the apex of tip cells [25, 35]. Whether PpRopGEFs are differentially involved in branch initiation and tip cell growth remains unknown.

Our results also suggest that a guidance cue exerted from polarity-dependent morphological change controls nuclear positioning. In *Arabidopsis*, lateral root initiation is accomplished by

Figure 3. Effects of *rop* Mutations on Cell Growth, Cell Shape, Gametophore Development, and Subapical Cell Branch Formation

(A) Colony growth in wild-type (WT) and *rop* mutant lines. Scale bar, 1 cm.

(B) Box-and-whisker plots of normalized colony sizes. Boxes show the interquartile range. Median and mean values are indicated by the crossline and "+," respectively. Nine colonies were used for quantification for each strain except the RNAi line (n = 32).

(C and D) Protonema cell morphology in WT and *rop* mutants. Scale bars, 100 μm (C); 20 μm (D).

(E) Gametophores in WT and *rop* mutants. Scale bar, 1 mm.

(F) Subapical cell division in the WT and *rop2, rop3, rop4* triple mutant (*rop2-4*) lines. Cells are labeled with Lifeact-mCherry and chloroplast autofluorescence. 0 min, NEB. d and θ indicate the distance of the division plane to the apical end and orientation of the division plane, respectively. Note that the division plane of bulged cells of *rop2-4* mutants is also affected. Scale bar, 20 μm.

(G) Kymographs showing nuclear migration in the WT and *rop* triple mutant. N, nucleus. Star, growing bulge. Note that the directional movement [1], but not the fast migration phase [2], is affected in the mutant. [3] indicates mitosis. Scale bars, 10 μm (horizontal), 1 h (vertical).

(H) Schematic illustration of nuclear dynamics in subapical cells. Three distinct phases are observable.

(I) Branch formation in 4-day-old regenerating protoplasts. Scale bar, 0.1 mm.

See also Figure S2 and Video S4.

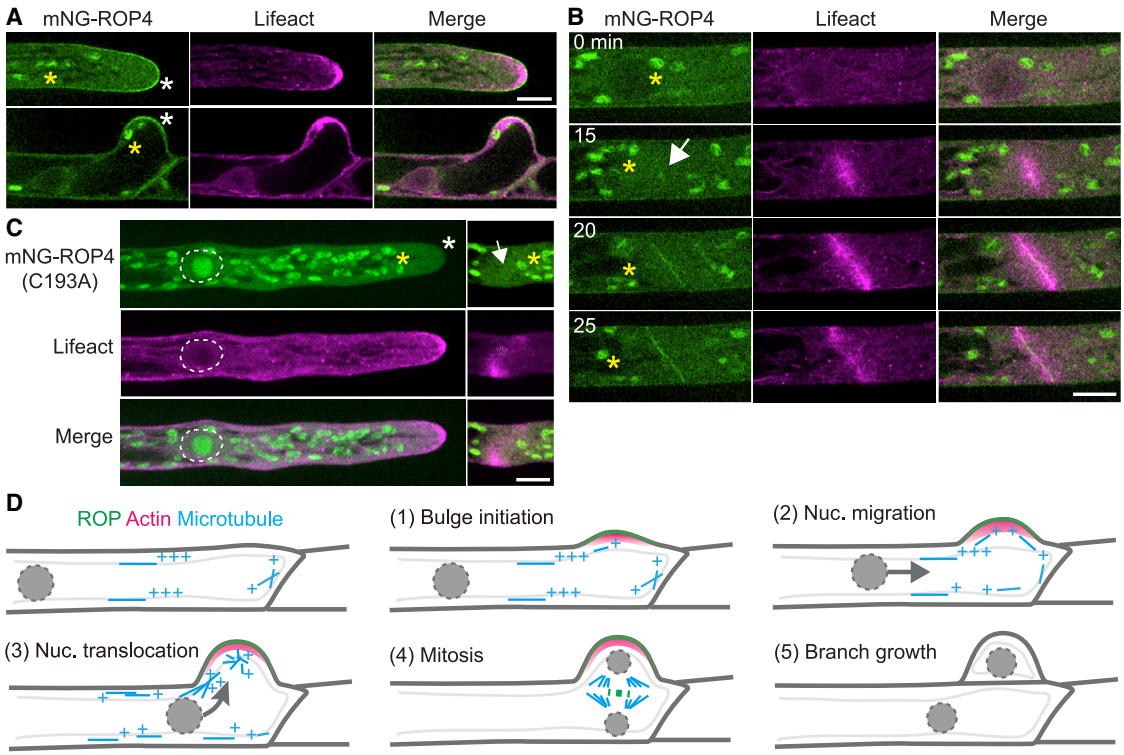

Figure 4. ROP4 Is Localized to the Apical Membrane and the Assembling Cell Plate

(A) Localization of mNeonGreen-ROP4 (mNG-ROP4) and Lifeact-mCherry in the tip cells (upper) and subapical cells (below). White stars indicate the membrane localization of mNG-ROP4. Yellow stars show chloroplast autofluorescence (the same in other panels).

(B) Localization of mNG-ROP4 and Lifeact-mCherry in a mitotic tip cell. 0 min, NEB. Arrow indicates the initial appearance of ROP4 on the assembling cell plate.

(C) Modifying the C-terminal CXXL motif (C193A) abolishes membrane localization of mNG-ROP4. White star and arrow indicate the loss of mNG-ROP localization at the apical membrane and cell plate. The mutated protein is localized in the nucleoli. Dotted circle, nucleus.

(D) A model of side-branch formation in *P. patens*. The plus ends of MTs are indicated by "+."

Scale bars, 10 μm (A–C). See also Figure S3 and Video S5.

the ACD of founder cells [4]. Their division asymmetry is achieved by polar nuclear migration, a process that coincides with cell expansion [36, 37]. MTs, F-actin, and auxin signaling are critical for cell expansion and nuclear migration [37]. It is unclear how cell morphological changes regulate nuclear positioning. In particular, the nucleus migrates longitudinally, while the cell expands in the lateral direction. Polarity regulators such as ROPs may play a role in this process. In non-branching systems, cell polarity and nuclear positioning are also important for ACD. In *Zea mays*, subsidiary mother cells divide asymmetrically by anchoring the nucleus to the cortex that faces the neighboring cells. This process depends on polarized localization of PAN1, ROPs, and an actin patch [38, 39]. MTs and actin are required for the initiation and maintenance of polar nuclear positioning, respectively [40]. In *Arabidopsis* stomata, the asymmetric division of meristemoid mother cells is triggered by an angiosperm-specific protein, BASL [41]. Interestingly, the nuclei of meristemoid mother cells are located toward the opposite direction of polar BASL localization. In *P. patens*, polarity-dependent morphological change underlies altered MT patterning and MT-dependent nuclear transport. These findings indicate that nuclear positioning and ACDs triggered by cell polarity and cytoskeleton are a fundamental mechanism to increase plant multicellularity. However, how nuclear positioning is coordinated with cell polarity remains unsolved at a molecular level. ROP GTPase is known to affect actin dynamics, which in turn alters MT dynamics [24]. A few proteins could potentially link actin and MTs. For example, KCH kinesin contains an actin-binding domain and drives retrograde nuclear movement [21]. Myosin VIII restricts branch formation and decorates both MT and actin structures [14, 42, 43]. The MT-severing protein Katanin acts downstream of ROP6-RIC1 to promote MT ordering [44]. Whether these factors contribute to nuclear migration during side-branching awaits future work.

STAR★METHODS

Detailed methods are provided in the online version of this paper and include the following:

- KEY RESOURCES TABLE
- RESOURCE AVAILABILITY
  - Lead Contact
  - Materials Availability
  - Data and Code Availability

SUPPLEMENTAL INFORMATION

Supplemental Information can be found online at https://doi.org/10.1016/j.cub.2020.05.022.

ACKNOWLEDGMENTS

We thank Dr. Mitsuyasu Hasebe for sharing the STEMIN1pro:NGG plasmid, and Dr. Elena Kozgunova for comments on this manuscript. This work is supported by JSPS KAKENHI (17H06471) to G.G. P.Y. is a recipient of a long-term postdoctoral fellowship from the Human Frontier Science Program (LT000611/2018-L).

AUTHOR CONTRIBUTIONS

G.G. and P.Y. conceived the project. P.Y. performed the experiments and analyzed the data. P.Y. and G.G. wrote the manuscript.

DECLARATION OF INTERESTS

The authors declare no competing interests.

Received: January 30, 2020
Revised: April 6, 2020
Accepted: May 6, 2020
Published: May 28, 2020

REFERENCES

1. Teichmann, T., and Muhr, M. (2015). Shaping plant architecture. Front. Plant Sci. *6*, 233.
2. Wang, S., Sekiguchi, R., Daley, W.P., and Yamada, K.M. (2017). Patterned cell and matrix dynamics in branching morphogenesis. J. Cell Biol. *216*, 559–570.
3. Barbier, F.F., Dun, E.A., Kerr, S.C., Chabikwa, T.G., and Beveridge, C.A. (2019). An update on the signals controlling shoot branching. Trends Plant Sci. *24*, 220–236.
4. Banda, J., Bellande, K., von Wangenheim, D., Goh, T., Guyomarc'h, S., Laplaze, L., and Bennett, M.J. (2019). Lateral root formation in Arabidopsis: a well-ordered LRexit. Trends Plant Sci. *24*, 826–839.
5. Coudert, Y., Harris, S., and Charrier, B. (2019). Design principles of branching morphogenesis in filamentous organisms. Curr. Biol. *29*, R1149–R1162.
6. Cove, D. (2005). The moss Physcomitrella patens. Annu. Rev. Genet. *39*, 339–358.
7. Nakaoka, Y., Miki, T., Fujioka, R., Uehara, R., Tomioka, A., Obuse, C., Kubo, M., Hiwatashi, Y., and Goshima, G. (2012). An inducible RNA interference system in Physcomitrella patens reveals a dominant role of augmin in phragmoplast microtubule generation. Plant Cell *24*, 1478–1493.
8. Wada, M. (1995). Nuclear behavior during branch formation in a centrifuged Adiantum protonema and the nuclear polarity. J. Plant Res. *108*, 501–509.
9. Jones, M., and Smirnoff, N. (2006). Nuclear dynamics during the simultaneous and sustained tip growth of multiple root hairs arising from a single root epidermal cell. J. Exp. Bot. *57*, 4269–4275.
10. Ketelaar, T., Faivre-Moskalenko, C., Esseling, J.J., de Ruijter, N.C.A., Grierson, C.S., Dogterom, M., and Emons, A.M.C. (2002). Positioning of nuclei in Arabidopsis root hairs: an actin-regulated process of tip growth. Plant Cell *14*, 2941–2955.
11. Nakamura, M., Claes, A.R., Grebe, T., Hermkes, R., Viotti, C., Ikeda, Y., and Grebe, M. (2018). Auxin and ROP GTPase signaling of polar nuclear migration in root epidermal hair cells. Plant Physiol. *176*, 378–391.
12. Doonan, J.H., Jenkins, G.I., Cove, D.J., and Lloyd, C.W. (1986). Microtubules connect the migrating nucleus to the prospective division site during side branch formation in the moss, Physcomitrella patens. Eur. J. Cell Biol. *41*, 157–164.
13. Doonan, J.H., Cove, D.J., and Lloyd, C.W. (1988). Microtubules and microfilaments in tip growth: evidence that microtubules impose polarity on protonemal growth in Physcomitrella patens. J. Cell Sci. *89*, 533–540.
14. Wu, S.-Z., and Bezanilla, M. (2018). Actin and microtubule cross talk mediates persistent polarized growth. J. Cell Biol. *217*, 3531–3544.
15. Finka, A., Schaefer, D.G., Saidi, Y., Goloubinoff, P., and Zrÿd, J.-P. (2007). In vivo visualization of F-actin structures during the development of the moss Physcomitrella patens. New Phytol. *174*, 63–76.
16. Quader, H., and Schnepf, E. (1989). Actin filament array during side branch initiation in protonema cells of the mossFunaria hygrometrica: an actin organizing center at the plasma membrane. Protoplasma *151*, 167–170.
17. Vidali, L., Augustine, R.C., Kleinman, K.P., and Bezanilla, M. (2007). Profilin is essential for tip growth in the moss Physcomitrella patens. Plant Cell *19*, 3705–3722.
18. Vidali, L., Rounds, C.M., Hepler, P.K., and Bezanilla, M. (2009). Lifeact-mEGFP reveals a dynamic apical F-actin network in tip growing plant cells. PLoS ONE *4*, e5744.
19. Hiwatashi, Y., Sato, Y., and Doonan, J.H. (2014). Kinesins have a dual function in organizing microtubules during both tip growth and cytokinesis in Physcomitrella patens. Plant Cell *26*, 1256–1266.
20. Yamada, M., Tanaka-Takiguchi, Y., Hayashi, M., Nishina, M., and Goshima, G. (2017). Multiple kinesin-14 family members drive microtubule minus end-directed transport in plant cells. J. Cell Biol. *216*, 1705–1714.
21. Yamada, M., and Goshima, G. (2018). The KCH kinesin drives nuclear transport and cytoskeletal coalescence to promote tip cell growth in *Physcomitrella patens*. Plant Cell *30*, 1496–1510.
22. Miki, T., Nishina, M., and Goshima, G. (2015). RNAi screening identifies the armadillo repeat-containing kinesins responsible for microtubule-dependent nuclear positioning in Physcomitrella patens. Plant Cell Physiol. *56*, 737–749.
23. Feiguelman, G., Fu, Y., and Yalovsky, S. (2018). ROP GTPases structure-function and signaling pathways. Plant Physiol. *176*, 57–79.
24. Burkart, G.M., Baskin, T.I., and Bezanilla, M. (2015). A family of ROP proteins that suppresses actin dynamics, and is essential for polarized growth and cell adhesion. J. Cell Sci. *128*, 2553–2564.
25. Eklund, D.M., Svensson, E.M., and Kost, B. (2010). Physcomitrella patens: a model to investigate the role of RAC/ROP GTPase signalling in tip growth. J. Exp. Bot. *61*, 1917–1937.
26. Collonnier, C., Epert, A., Mara, K., Maclot, F., Guyon-Debast, A., Charlot, F., White, C., Schaefer, D.G., and Nogué, F. (2017). CRISPR-Cas9-mediated efficient directed mutagenesis and RAD51-dependent and RAD51-independent gene targeting in the moss Physcomitrella patens. Plant Biotechnol. J. *15*, 122–131.
27. Yi, P., and Goshima, G. (2020). Transient cotransformation of CRISPR/Cas9 and oligonucleotide templates enables efficient editing of target loci in Physcomitrella patens. Plant Biotechnol. J. *18*, 599–601.
28. Ito, K., Ren, J., and Fujita, T. (2014). Conserved function of Rho-related Rop/RAC GTPase signaling in regulation of cell polarity in Physcomitrella patens. Gene *544*, 241–247.
29. Kubo, M., Imai, A., Nishiyama, T., Ishikawa, M., Sato, Y., Kurata, T., Hiwatashi, Y., Reski, R., and Hasebe, M. (2013). System for stable β-estradiol-inducible gene expression in the moss Physcomitrella patens. PLoS ONE *8*, e77356.

30. Ishikawa, M., Morishita, M., Higuchi, Y., Ichikawa, S., Ishikawa, T., Nishiyama, T., Kabeya, Y., Hiwatashi, Y., Kurata, T., Kubo, M., et al. (2019). Physcomitrella STEMIN transcription factor induces stem cell formation with epigenetic reprogramming. Nat. Plants *5*, 681–690.

31. Shaner, N.C., Lambert, G.G., Chammas, A., Ni, Y., Cranfill, P.J., Baird, M.A., Sell, B.R., Allen, J.R., Day, R.N., Israelsson, M., et al. (2013). A bright monomeric green fluorescent protein derived from Branchiostoma lanceolatum. Nat. Methods *10*, 407–409.

32. Stöckle, D., Herrmann, A., Lipka, E., Lauster, T., Gavidia, R., Zimmermann, S., and Müller, S. (2016). Putative RopGAPs impact division plane selection and interact with kinesin-12 POK1. Nat. Plants *2*, 16120.

33. Bascom, C., Jr., Burkart, G.M., Mallett, D.R., O'Sullivan, J.E., Tomaszewski, A.J., Walsh, K., and Bezanilla, M. (2019). Systematic survey of the function of ROP regulators and effectors during tip growth in the moss Physcomitrella patens. J. Exp. Bot. *70*, 447–457.

34. Denninger, P., Reichelt, A., Schmidt, V.A.F., Mehlhorn, D.G., Asseck, L.Y., Stanley, C.E., Keinath, N.F., Evers, J.-F., Grefen, C., and Grossmann, G. (2019). Distinct RopGEFs successively drive polarization and outgrowth of root hairs. Curr. Biol. *29*, 1854–1865.e5.

35. Le Bail, A., Schulmeister, S., Perroud, P.-F., Ntefidou, M., Rensing, S.A., and Kost, B. (2019). Analysis of the localization of fluorescent PpROP1 and PpROP-GEF4 fusion proteins in moss protonemata based on genomic "knock-in" and estradiol-titratable expression. Front. Plant Sci. *10*, 456.

36. De Rybel, B., Vassileva, V., Parizot, B., Demeulenaere, M., Grunewald, W., Audenaert, D., Van Campenhout, J., Overvoorde, P., Jansen, L., Vanneste, S., et al. (2010). A novel aux/IAA28 signaling cascade activates GATA23-dependent specification of lateral root founder cell identity. Curr. Biol. *20*, 1697–1706.

37. Vilches Barro, A., Stöckle, D., Thellmann, M., Ruiz-Duarte, P., Bald, L., Louveaux, M., von Born, P., Denninger, P., Goh, T., Fukaki, H., et al. (2019). Cytoskeleton dynamics are necessary for early events of lateral root initiation in Arabidopsis. Curr. Biol. *29*, 2443–2454.e5.

38. Cartwright, H.N., Humphries, J.A., and Smith, L.G. (2009). PAN1: a receptor-like protein that promotes polarization of an asymmetric cell division in maize. Science *323*, 649–651.

39. Humphries, J.A., Vejlupkova, Z., Luo, A., Meeley, R.B., Sylvester, A.W., Fowler, J.E., and Smith, L.G. (2011). ROP GTPases act with the receptor-like protein PAN1 to polarize asymmetric cell division in maize. Plant Cell *23*, 2273–2284.

40. Panteris, E., Apostolakos, P., and Galatis, B. (2006). Cytoskeletal asymmetry in Zea mays subsidiary cell mother cells: a monopolar prophase microtubule half-spindle anchors the nucleus to its polar position. Cell Motil. Cytoskeleton *63*, 696–709.

41. Dong, J., MacAlister, C.A., and Bergmann, D.C. (2009). BASL controls asymmetric cell division in Arabidopsis. Cell *137*, 1320–1330.

42. Wu, S.-Z., Ritchie, J.A., Pan, A.-H., Quatrano, R.S., and Bezanilla, M. (2011). Myosin VIII regulates protonemal patterning and developmental timing in the moss Physcomitrella patens. Mol. Plant *4*, 909–921.

43. Wu, S.-Z., and Bezanilla, M. (2014). Myosin VIII associates with microtubule ends and together with actin plays a role in guiding plant cell division. eLife *3*, e03498.

44. Lin, D., Cao, L., Zhou, Z., Zhu, L., Ehrhardt, D., Yang, Z., and Fu, Y. (2013). Rho GTPase signaling activates microtubule severing to promote microtubule ordering in Arabidopsis. Curr. Biol. *23*, 290–297.

45. Schindelin, J., Arganda-Carreras, I., Frise, E., Kaynig, V., Longair, M., Pietzsch, T., Preibisch, S., Rueden, C., Saalfeld, S., Schmid, B., et al. (2012). Fiji: an open-source platform for biological-image analysis. Nat. Methods *9*, 676–682.

46. Jakobs, M.A., Dimitracopoulos, A., and Franze, K. (2019). KymoButler, a deep learning software for automated kymograph analysis. eLife *8*, e42288.

47. Ashton, N.W., and Cove, D.J. (1977). The isolation and preliminary characterisation of auxotrophic and analogue resistant mutants of the moss, Physcomitrella patens. Mol. Gen. Genet. *154*, 87–95.

48. Yamada, M., Miki, T., and Goshima, G. (2016). Imaging mitosis in the moss Physcomitrella patens. Methods Mol. Biol. *1413*, 263–282.

49. Kozgunova, E., and Goshima, G. (2019). A versatile microfluidic device for highly inclined thin illumination microscopy in the moss Physcomitrella patens. Sci. Rep. *9*, 15182.

STAR★METHODS

KEY RESOURCES TABLE

REAGENT or RESOURCE	SOURCE	IDENTIFIER
Antibodies		
Rabbit polyclonal anti-GFP	Gohta Goshima lab	"Nishi"
Mouse monoclonal anti-Tubulin (clone DM1A)	Sigma-Aldrich	Cat#T9026; RRID: AB_477593
Rat monoclonal(GF090R) anti-GFP, agarose conjugate	Nacalai Tesque	Cat#06083-05
Bacterial and Virus Strains		
E. coli strain DH5α	Widely distributed	N/A
Chemicals, Peptides, and Recombinant Proteins		
Oryzalin	AccuStandard	Cat#538-56741
Latrunculin A	Fujifilm	Cat#125-04363
β-estradiol	Fujifilm	Cat#056-04044
Critical Commercial Assays		
In-Fusion HD Cloning Kit	Takara	Cat#639635
KOD FX Neo Polymerase Kit	Toyobo	Cat#KFX-101
Deposited Data		
Codon-optimized mNeonGreen plasmid	This manuscript	Addgene #137082
Experimental Models: Organisms/Strains		
P. patens: Strain GH#5: GFP-α-tubulin, H2B-RFP	[7]	GH#5
P. patens: Strain GPH379: mCherry-α-tubulin, EB1-Citrine	[20]	GPH379
P. patens: Strain GPH407: Lifeact-mCherry	This manuscript	GPH407
P. patens: Strain GPH690: Lifeact-mCherry, *rop3*(frameshift)	This manuscript	GPH690
P. patens: Strain GPH689: Lifeact-mCherry, *rop3*(Δ5aa), *rop4*(Δ5aa)	This manuscript	GPH689
P. patens: Strain GPH728: Lifeact-mCherry, *rop2*(deletion), *rop3*(frameshift)	This manuscript	GPH728
P. patens: Strain GPH777: Lifeact-mCherry, *rop1*(Δsplicing), *rop3*(frameshift)	This manuscript	GPH777
P. patens: Strain GPH729: Lifeact-mCherry, *rop1*(Δsplicing), *rop2*(deletion), *rop3*(frameshift)	This manuscript	GPH729
P. patens: Strain GPH731: Lifeact-mCherry, *rop1*(Δsplicing), *rop2*(deletion), *rop3*(frameshift)	This manuscript	GPH731
P. patens: Strain GPH778: Lifeact-mCherry, *rop2*(Δ3aa), *rop3*(frameshift), *rop4*(Δ5aa)	This manuscript	GPH778
P. patens: Strain GPH733: Lifeact-mCherry, *rop2*(Δ3aa), *rop3*(frameshift), *rop4*(6bp/58bp del/ins)	This manuscript	GPH733
P. patens: Strain GPH810: Lifeact-mCherry, *rop1*(Δsplicing), *rop2*(deletion), *rop3*(frameshift), *rop4* RNAi	This manuscript	GPH810
P. patens: Strain GPH892: Lifeact-mCherry, *rop1*(Δsplicing), *rop2*(deletion), *rop3*(frameshift), *rop4*(W100R)	This manuscript	GPH892
P. patens: Strain GPH796: InEx-Cerulean-ROP4, *rop2*(Δ3aa), *rop3*(frameshift), *rop4*(6bp/58bp del/ins)	This manuscript	GPH796
P. patens: Strain GPH797: InEx-Cerulean-ROP1, *rop2*(Δ3aa), *rop3*(frameshift), *rop4*(6bp/58bp del/ins)	This manuscript	GPH797
P. patens: Strain GPH691: Lifeact-mCherry, ROP4-Citrine	This manuscript	GPH691
P. patens: Strain GPH692: Lifeact-mCherry, ROP4-mNeonGreen	This manuscript	GPH692
P. patens: Strain GPH734: Lifeact-mCherry, mNeonGreen-ROP4	This manuscript	GPH734
P. patens: Strain GPH849: mNeonGreen-ROP4, mCherry-REN	This manuscript	GPH849
P. patens: Strain GPH925: Lifeact-mCherry, mNeonGreen-ROP4(C193A)	This manuscript	GPH925
P. patens: Strain GPH962: Lifeact-mCherry, GFP-α-tubulin	This manuscript	GPH962

(*Continued on next page*)

Continued

REAGENT or RESOURCE	SOURCE	IDENTIFIER
Oligonucleotides		
rop1 CRISPR target: CTCGGATTATGGGATACAGC (AGG)	This manuscript	N/A
rop2 CRISPR target: ACTGTAGGAGATGGAGCAGT (CGG)	This manuscript	N/A
rop3 CRISPR target: TACTGTAGGAGATGGAGCTG (TGG)	This manuscript	N/A
rop4 CRISPR target: AAGTGCGTGACTGTTGGAGA (TGG)	This manuscript	N/A
Software and Algorithms		
Fiji	[45]	https://imagej.net/Fiji
GraphPad Prism	GraphPad Software	N/A
Illustrator	Adobe	N/A
KymoButler	[46]	https://www.wolframcloud.com/objects/deepmirror/Projects/KymoButler/KymoButlerForm

RESOURCE AVAILABILITY

Lead Contact

Further information and requests for resources and reagents should be directed to and will be fulfilled by the Lead Contact, Peishan Yi (yi.peishan@a.mbox.nagoya-u.ac.jp).

Materials Availability

The codon-optimized mNeonGreen plasmid generated in this study has been deposited to Addgene (cat# 137082).

Data and Code Availability

This study did not generate/analyze any datasets.

EXPERIMENTAL MODEL AND SUBJECT DETAILS

Moss Strains and Growth Conditions

All strains were derived from the Gransden ecotype of *Physcomitrella patens* [47], and were cultured at 25°C on standard BCDAT plates with continuous light illumination [48]. Detailed information of strain genotype is available in the Key Resources Table.

METHOD DETAILS

Molecular Biology

CRISPR targets of *rop* genes were manually selected at the first or second exons with low off-target rate against the *P. patens* genome. All target sequences were synthesized in the form of single-stranded oligos, annealed to form double-stranded oligos, and were ligated into the *Bsa*I site of pCasGuide/pUC18 [26]. The final single-guide RNA (sgRNA) plasmid was constructed by inserting the four sgRNA cassettes targeting *rop1-rop4* into a Nourseothricin resistant plasmid using In-Fusion HD Cloning Kit (Takara). The mNeonGreen sequence (GenBank: KC295282) was codon-optimized for expression in *Arabidopsis* (Addgene:137082) and synthesized by Integrated DNA Technologies, Inc. The homology sequences spanning 1.1–1.2 kb 5′- and 3′- ends were used for endogenous tagging of ROP4. For C-terminal tagging, the insertional fragment following ROP coding sequence contains an in-frame linker, a Citrine/mNeonGreen coding sequence, a *nos* terminator, and a Hygromycin B resistant cassette. For N-terminal tagging, a sequence encoding a Flag tag and the mNeonGreen protein, together with a short linker, was added immediately after the ROP4 start codon. The plasmid for inducible expression of ROP1 or ROP4 was generated by cloning a Cerulean-ROP4 fragment into the pPGX8 vector using Gateway Cloning Kit (Invitrogen) [29]. The mCherry-REN plasmid was constructed by inserting the mCherry-REN fragment into the pMN601 overexpression vector under the control of *EF1*α promoter.

Transformation

All transformations were performed by following the PEG-mediated protoplast transformation protocol as described before [48]. Briefly, protoplasts were collected from 2% driselase-digested protonemata, washed with 8% mannitol, and resuspended in the MMM medium. Subsequently, 0.5 × 10^6 protoplasts were mixed with the PEG solution and DNA constructs, incubated at 45°C for 5 min and then at 20°C for 10 min, and diluted with protoplast liquid medium. After overnight culturing in the dark, cells were collected into the PRM-T medium and spread onto cellophane-laid PRM plates. Regenerated colonies were selected on selective

plates and subjected to genotyping and sequencing after recovering on BCDAT plates for appropriate days. For CRISPR knockout, circular sgRNA and pAct-Cas9 plasmids (each 10 μg) were transiently co-transformed into the Lifeact-mCherry line. Positive lines without illegitimate integration were selected and confirmed by the resistance test. For endogenous tagging and overexpression, 30 μg linearized plasmids were transformed into appropriate mother lines after ethanol-precipitation based purification. Genotyping was performed using the KOD FX Neo Polymerase Kit (Toyobo).

Imaging and Data Processing

Colony growth assay was performed by culturing 1-week old single colonies after protoplast regeneration for two weeks on BCDAT plates. Colony images were taken by a C-765 Ultra Zoom digital camera (Olympus). For oryzalin treatment, a previously established transgenic line labeled with GFP-tubulin and histone-RFP was used for imaging [7]. For latrunculin A treatment, a new transgenic line expressing brighter GFP-tubulin and histone-RFP was used. In the long-term time-lapse imaging experiments, protonema tissues were cultured in 6-well glass-bottom dishes with BCD agarose medium for 5–7 days. Images were taken by a Nikon TE2000-E microscope equipped with a 10 × 0.45 NA lens, a Zyla 4.2P CMOS camera (Andor), and a Nikon Intensilight Epi-fluorescence Illuminator at an interval of 10 min with in-between white light. For high-resolution imaging, protonema tissues were inoculated in 35-mm glass-bottom dishes supplemented with BCD agarose medium. The imaging system comprised a Nikon Ti microscope, a CSU-X1 spinning disk confocal scanner unit (Yokogawa), an EMCCD camera (ImagEM, Hamamatsu), appropriate lenses (40 × 1.30 NA, 60 × 1.2 NA, or 100 × 1.45 NA), and 561-nm and 488-nm laser lines (LDSYS-488/561-50-YHQSP3, Pneum). The oblique illumination fluorescence microscopy system included a Nikon Ti microscope equipped with total internal reflection fluorescence unit, 100 × 1.49-NA lens, GEMINI split view (Hamamatsu Photonics), and EMCCD camera Evolve (Roper). Sonicated moss protonemata were loaded into the 15-μm channels of polydimethylsiloxane microdevices and cultured in liquid BCD medium for 6–7 days before oblique illumination microscopy [49]. Images were acquired under the control of NIS-Elements software (Nikon) at an interval of 1–5 min for mitosis and cell growth, at an interval of 3–5 s for EB1 dynamics, and at an interval of 1 s for oblique illumination microscopy. Raw data processing and measurement were performed using the Fiji software [45]. To measure cell length, the average length of caulonemal tip cell and the first two subapical cells in wild-type and *rop* triple mutant lines were used. These results were not significantly different from those by quantifying the first subapical cell alone. The length of the individual tip and subapical cells were measured and pooled in strong mutant lines as they could not grow normal caulonema cells. Cell growth rate and nuclear migration speed were measured from kymographs. To quantify EB1 dynamics, kymographs were generated from lines along the apical-basal axis in the lateral cytoplasms of subapical cells by using the Multi Kymograph plugin with a 5-pixel line width. The number of comets in the forward and reverse directions was counted manually. Another online tool KymoButler was also used to perform the quantification but revealed no significant difference [46].

Drug Treatment

In the long-term imaging experiments, the agarose medium surrounding moss colonies was removed. Liquid BCD medium (500 μL) containing 1 μM oryzalin or 5 μM latrunculin A was directly added to immerse the entire moss colonies before imaging. For high-resolution imaging, moss colonies were pre-incubated with 1 mL sterilized water for > 30 min. Afterward, water was replaced with a 300 μL liquid BCD medium, which contained an appropriate amount of latrunculin A at a final concentration of 25 μM. In control cells, equal volumes of DMSO were added. For oblique illumination microscopy, the liquid medium in microdevice samples was removed and replaced by drug solutions using a syringe. Protein expression for immunoblotting was induced by transferring 4–6-day-old sonicated protonemata to BCDAT plates supplemented with 1 μM β-estradiol and culturing them for another 2 days. Small pieces of moss protonemata were cultured directly on β-estradiol-containing plates for 10 days before colony imaging.

Immunoprecipitation and Western Blotting

Sonicated protonemata were ground in liquid nitrogen and resuspended in SDS-PAGE sample buffer for western blotting or in lysis buffer (50 mM Tris-HCl pH 7.5, 150 mM NaCl, 2% Triton X-100, 1 × proteinase inhibitor cocktail, 1 mM PMSF) for immunoprecipitation. In the immunoprecipitation experiment, the supernatant of centrifuged lysate was incubated with 10–20 μl anti-GFP antibody beads (Rat IgG2a, Monoclonal (GF090R), Nacalai Tesque.) at 4°C for 1 h. Beads were washed three times with wash buffer (50 mM Tris-HCl pH 7.5, 150 mM NaCl, 0.1% Triton X-100, 1 × proteinase inhibitor cocktail, 1 mM PMSF) and boiled in a 20 μL SDS-PAGE sample buffer. Boiled samples were subject to SDS-PAGE using 5%–20% premade acrylamide gel (Bio-Rad) followed by immunoblotting using a homemade primary anti-GFP antibody (rabbit, 1:250) and a horseradish peroxidase-conjugated anti-rabbit secondary antibody (1:4000).

QUANTIFICATION AND STATISTICAL ANALYSIS

The exact values of sample size (n) and estimates of variability (mean ± SD or ± SEM) are shown in the main text and figure legends where necessary. Statistical analyses were performed in GraphPad Prism using a two-tailed t test comparison and significant difference between groups was determined when the p value was less than 0.05.

Current Biology, Volume *30*

Supplemental Information

Rho of Plants GTPases and Cytoskeletal Elements Control Nuclear Positioning and Asymmetric Cell Division during *Physcomitrella patens* Branching

Peishan Yi and Gohta Goshima

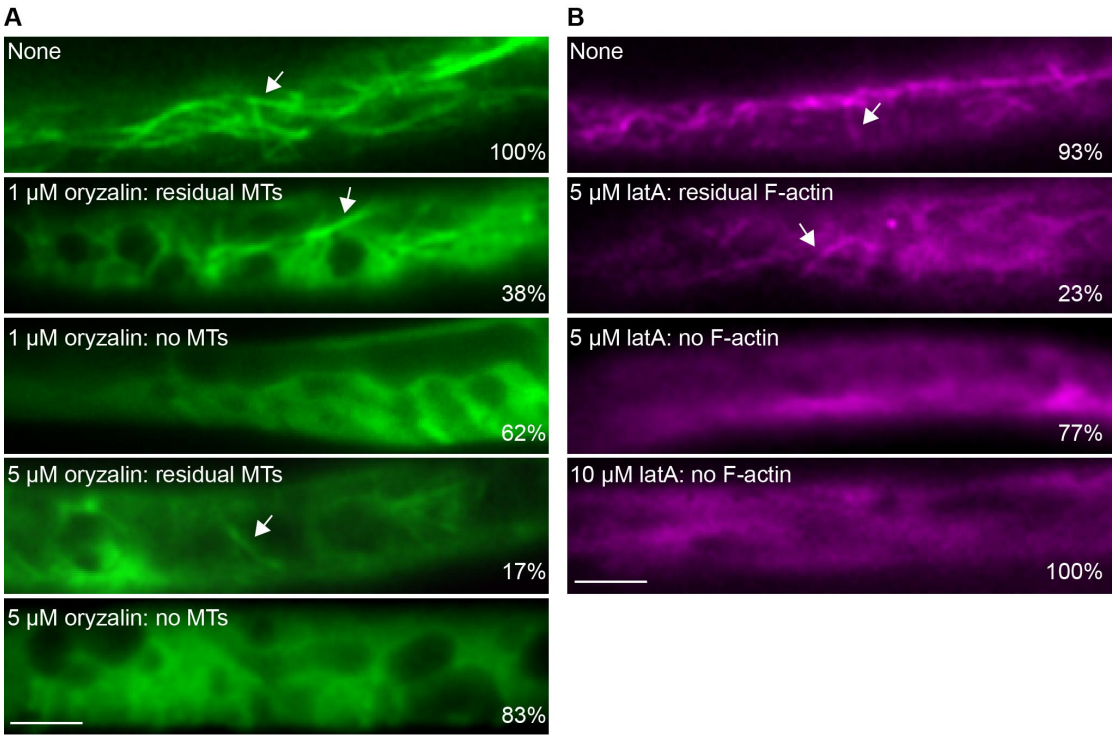

Figure S1. Effects of oryzalin and latrunculin A on microtubule and actin structures, Related to Figure 1 and 2.

(A) Microtubules in oryzalin-treated caulonema cells. Percentages of cells observed for each category are shown. n = 24, 40, and 29 for no treatment, 1 μM oryzalin, and 5 μM orzyzalin, respectively. Arrows indicate microtubules. (B) Actin filaments in latrunculin A (latA)-treated caulonema cells. Percentages of cells observed for each category are shown. n = 45, 31, and 27 for no treatment, 5 μM latA, and 10 μM latA, respectively. Arrows indicate actin filaments. Scale bars: 5 μm (A–B).

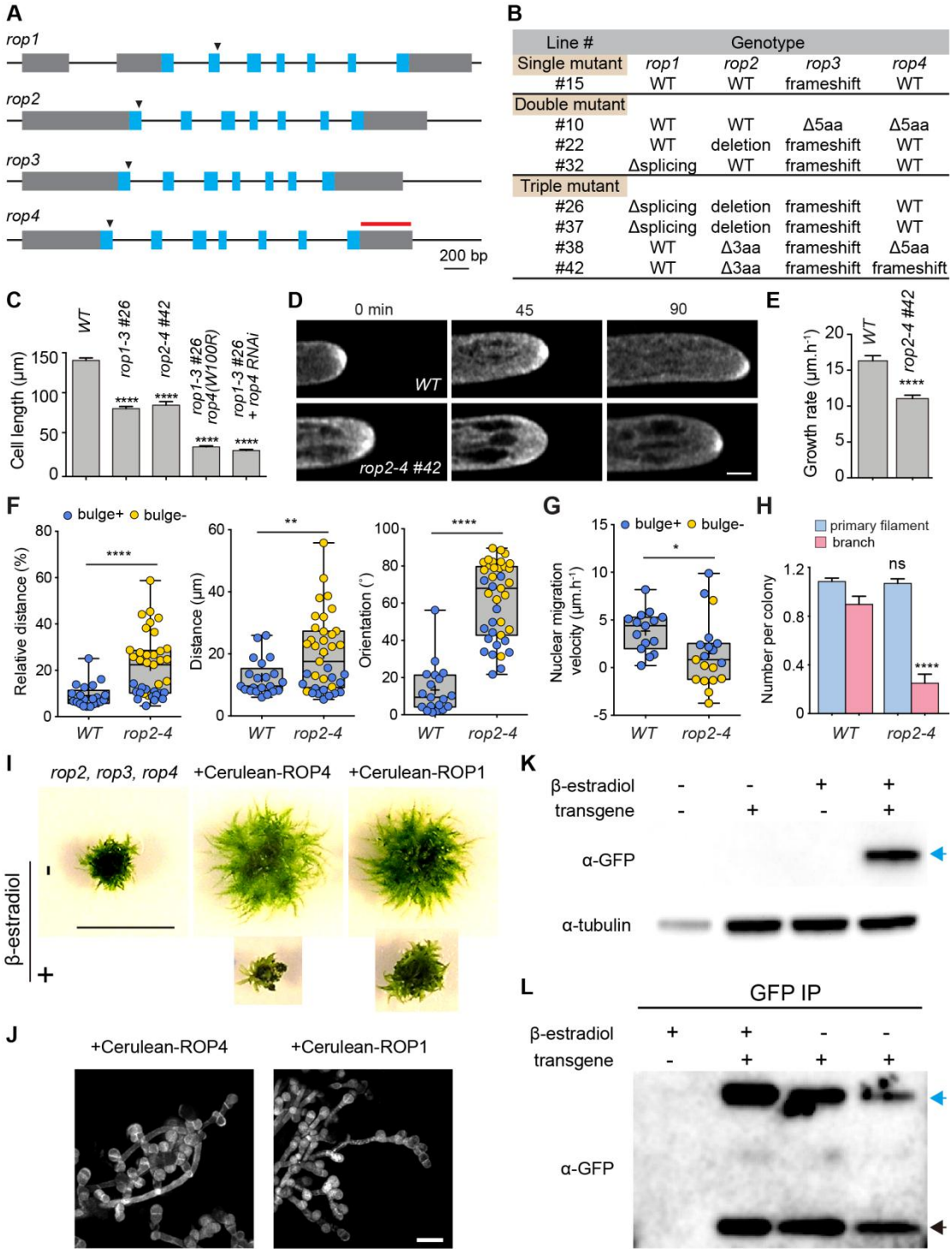

Line #	Genotype			
Single mutant	*rop1*	*rop2*	*rop3*	*rop4*
#15	WT	WT	frameshift	WT
Double mutant				
#10	WT	WT	Δ5aa	Δ5aa
#22	WT	deletion	frameshift	WT
#32	Δsplicing	WT	frameshift	WT
Triple mutant				
#26	Δsplicing	deletion	frameshift	WT
#37	Δsplicing	deletion	frameshift	WT
#38	WT	Δ3aa	frameshift	Δ5aa
#42	WT	Δ3aa	frameshift	frameshift

Figure S2. Construction of *rop* mutant lines and phenotypes of *rop* mutants, Related to Figure 3.

(A) Gene structures of *rop1-rop4*. Arrowheads indicate the site of CRISPR targets used for knockout. Red line shows the 3'UTR region used for RNAi. Scale bar: 200 bp. (B) Genotypes of *rop* mutant lines. In-frame deletions of three or five amino acids are shown as Δ3aa and Δ5aa, respectively. (C) Quantification of cell length. Mean ± SEM. n = 40, 27, 14, 32, 40, respectively, of stains from left to right. ****, $p < 0.0001$. (D) Tip

cell growth in WT and *rop2-4* mutant. Scale bar: 10 μm. (E) Quantification of growth rate. Mean ± SEM. WT, n = 66; *rop2-4*, n = 36. ****, p < 0.0001. (F) Box-and-whisker plots of division site positioning along the apical-basal axis and orientation of the division plane. Boxes show the interquartile range. Median and mean values are indicated by the crossline and "+", respectively. Bulged and non-bulged cells are colored in blue and yellow, respectively. WT, n = 21 (left and middle) and 19 (right). *rop2-4*, n = 37 (left and middle) and 39 (right). ****, p < 0.0001. **, p < 0.01. (G) Quantification of nuclear migration velocity during the directional-movement phase. WT, n = 15. *rop2-4*, n = 19. *, p < 0.05. (H) Quantification of the number of primary filaments and branches in 4-day-old regenerating protoplasts. WT, n = 106. *rop2-4*, n = 44. Mean ± SEM. ns, not significant. ****, p < 0.0001. (I) Basal expression of ROP1 and ROP4 without β-estradiol addition rescues protonema growth in the *rop2-4* triple mutant, while induced overexpression results in retarded growth. Scale bar: 1 cm. (J) Round cells caused by overexpression of ROP1 and ROP4. Scale bar: 100 μm. (K) Western blotting of Cerulean-ROP1 using anti-GFP antibody, which recognizes Cerulean. Without β-estradiol induction, Cerulean-ROP1 is not detectable (lane 2). Blue arrow indicates the Cerulean-ROP1 band. (L) Without β-estradiol induction, Cerulean-ROP4 (lane 3) and Cerulean-ROP1 (lane 4) are detected after immunoprecipitation followed by western blotting. Induced expression of Cerulean-ROP1 is used as a positive control (lane 2). Blue and black arrows indicate the Cerulean-ROP bands and the Cerulean-only band caused by protein degradation, respectively.

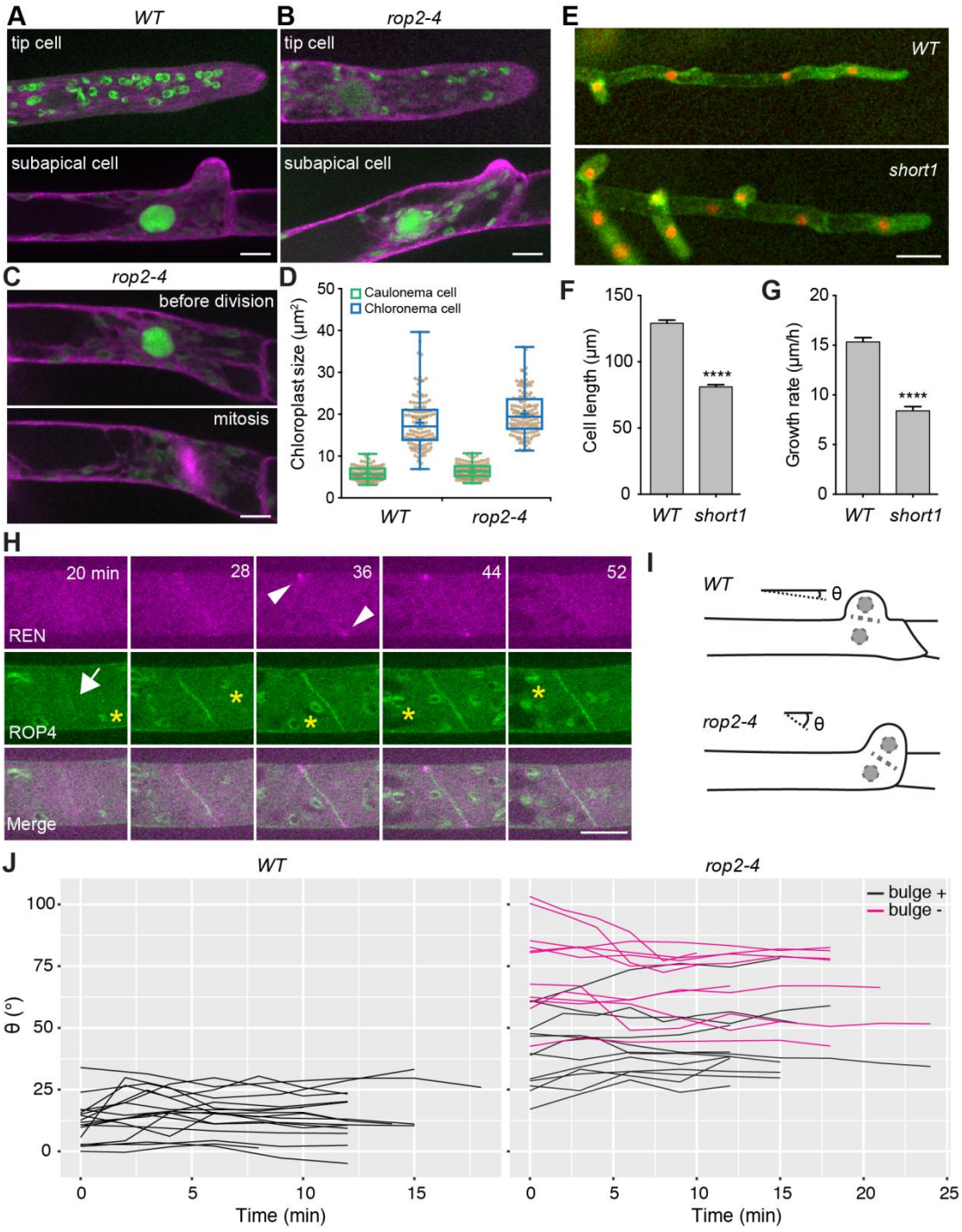

Figure S3. Division phenotypes of *rop2-4* subapical cells are not caused by cell fate change, cell shape alteration, or loss of phragmoplast guidance, Related to Figure 4.

(A-C) STEMIN1pro:NGG expression in WT and *rop2-4* mutant cells. Scale bar: 10 μm. (D) Box-and-whisker plots of chloroplast sizes in the caulonema and chloronema cells. Boxes show the interquartile range. Median and mean values are indicated by the crossline and "+", respectively. WT, n = 101 (caulonema) and 121 (chloronema);

rop2-4, n = 110 (caulonema) and 127 (chloronema). (E) The *short1* mutant exhibits short protonema cells but no subapical cell division abnormality. Scale bar: 50 μm. (F) Quantification of cell length. Mean ± SEM. WT, n = 48; *short1*, n = 72. ****, $p < 0.0001$. (G) Quantification of growth rate in tip cells. Mean ± SEM. WT, n = 85; *short1*, n = 75. ****, $p < 0.0001$. (H) Localization of mNG-ROP4 and REN in a mitotic tip cell. Time after NEB is shown. Arrow indicates the initial appearance of ROP4 on the assembling cell plate. Arrowheads indicate the accumulation of REN on the cortical division zone. Stars indicate chloroplast autofluorescence. Scale bar: 10 μm. See also Video S5. (I) Schematic illustration of phragmoplast orientation. (J) Direction of phragmoplast expansion along cytokinesis progression. Each line indicates a single cell.